

Magnitude and phase-resolved infrared vibrational nanospectroscopy with a swept quantum cascade laser

Edward Yoxall,¹ Martin Schnell,¹ Stefan Mastel,¹ and Rainer Hillenbrand^{2,3,*}

¹*CIC NanoGUNE, E-20018, Donostia – San Sebastian, Spain*

²*CIC NanoGUNE and EHU/UPV, E-20018, Donostia – San Sebastian, Spain*

³*IKERBASQUE, Basque Foundation for Science, E-48011 Bilbao, Spain*

r.hillenbrand@nanogune.eu

Abstract: We demonstrate a method of rapidly acquiring background-free infrared near-field spectra by combining magnitude and phase resolved scattering-type scanning near-field optical microscopy (s-SNOM) with a wavelength-swept quantum cascade laser (QCL). Background-free measurement of both near-field magnitude and phase allows for direct comparison with far-field absorption spectra, making the technique particularly useful for rapid and straightforward nanoscale material identification. Our experimental setup is based on the commonly used pseudo-heterodyne detection scheme, which we modify by operating the interferometer in the white light position; we show this adjustment to be critical for measurement repeatability. As a proof-of-principle experiment we measure the near-field spectrum between 1690 and 1750 cm^{-1} of a PMMA disc with a spectral resolution of 1.5 cm^{-1} . We finish by chemically identifying two fibers on a sample surface by gathering their spectra between 1570 and 1750 cm^{-1} , each with a measurement time of less than 2.5 minutes. Our method offers the possibility of performing both nanoscale-resolved point spectroscopy and monochromatic imaging with a single laser that is capable of wavelength-sweeping.

©2015 Optical Society of America

OCIS codes: (180.4243) Near-field microscopy; (140.5965) Semiconductor lasers, quantum cascade; (300.6340) Spectroscopy, infrared; (240.6490) Spectroscopy, surface; (310.6628) Subwavelength structures, nanostructures.

References and links

1. F. Keilmann and R. Hillenbrand, “Near-field microscopy by elastic light scattering from a tip,” *Philos. Trans. R. Soc., A* **362**(1817), 787–805 (2004).
2. B. Knoll and F. Keilmann, “Near-field probing of vibrational absorption for chemical microscopy,” *Nature* **399**(6732), 134–137 (1999).
3. T. Taubner, R. Hillenbrand, and F. Keilmann, “Nanoscale polymer recognition by spectral signature in scattering infrared near-field microscopy,” *Appl. Phys. Lett.* **85**(21), 5064–5066 (2004).
4. M. B. Raschke, L. Molina, T. Elsaesser, D. H. Kim, W. Knoll, and K. Hinrichs, “Apertureless near-field vibrational imaging of block-copolymer nanostructures with ultrahigh spatial resolution,” *ChemPhysChem* **6**(10), 2197–2203 (2005).
5. R. Hillenbrand, T. Taubner, and F. Keilmann, “Phonon-enhanced light matter interaction at the nanometre scale,” *Nature* **418**(6894), 159–162 (2002).
6. S. Dai, Z. Fei, Q. Ma, A. S. Rodin, M. Wagner, A. S. McLeod, M. K. Liu, W. Gannett, W. Regan, K. Watanabe, T. Taniguchi, M. Thiemens, G. Dominguez, A. H. C. Neto, A. Zettl, F. Keilmann, P. Jarillo-Herrero, M. M. Fogler, and D. N. Basov, “Tunable phonon polaritons in atomically thin van der Waals crystals of boron nitride,” *Science* **343**(6175), 1125–1129 (2014).
7. J. M. Stiegler, A. J. Huber, S. L. Diedenhofen, J. Gómez Rivas, R. E. Algra, E. P. A. M. Bakkers, and R. Hillenbrand, “Nanoscale free-carrier profiling of individual semiconductor nanowires by infrared near-field nanoscopy,” *Nano Lett.* **10**(4), 1387–1392 (2010).
8. R. Esteban, R. Vogelgesang, J. Dorfmueller, A. Dmitriev, C. Rockstuhl, C. Etrich, and K. Kern, “Direct near-field optical imaging of higher order plasmonic resonances,” *Nano Lett.* **8**(10), 3155–3159 (2008).
9. R. L. Olmon, P. M. Krenz, A. C. Jones, G. D. Boreman, and M. B. Raschke, “Near-field imaging of optical antenna modes in the mid-infrared,” *Opt. Express* **16**(25), 20295–20305 (2008).

10. D.-S. Kim, J. Heo, S.-H. Ahn, S. W. Han, W. S. Yun, and Z. H. Kim, "Real-space mapping of the strongly coupled plasmons of nanoparticle dimers," *Nano Lett.* **9**(10), 3619–3625 (2009).
11. M. Esslinger, J. Dorfmueller, W. Khunsin, R. Vogelgesang, and K. Kern, "Background-free imaging of plasmonic structures with cross-polarized apertureless scanning near-field optical microscopy," *Rev. Sci. Instrum.* **83**(3), 033704 (2012).
12. P. Alonso-González, P. Albella, F. Golmar, L. Arzubiaiga, F. Casanova, L. E. Hueso, J. Aizpurua, and R. Hillenbrand, "Visualizing the near-field coupling and interference of bonding and anti-bonding modes in infrared dimer nanoantennas," *Opt. Express* **21**(1), 1270–1280 (2013).
13. M. Brehm, T. Taubner, R. Hillenbrand, and F. Keilmann, "Infrared spectroscopic mapping of single nanoparticles and viruses at nanoscale resolution," *Nano Lett.* **6**(7), 1307–1310 (2006).
14. F. Ballout, H. Krassen, I. Kopf, K. Ataka, E. Bründermann, J. Heberle, and M. Havenith, "Scanning near-field IR microscopy of proteins in lipid bilayers," *Phys. Chem. Chem. Phys.* **13**(48), 21432–21436 (2011).
15. M. Paulite, Z. Fakhraai, I. T. S. Li, N. Gunari, A. E. Tanur, and G. C. Walker, "Imaging secondary structure of individual amyloid fibrils of a β 2-microglobulin fragment using near-field infrared spectroscopy," *J. Am. Chem. Soc.* **133**(19), 7376–7383 (2011).
16. I. Amenabar, S. Poly, W. Nuansing, E. H. Hubrich, A. A. Govyadinov, F. Huth, R. Krutokhvostov, L. Zhang, M. Knez, J. Heberle, A. M. Bittner, and R. Hillenbrand, "Structural analysis and mapping of individual protein complexes by infrared nanospectroscopy," *Nat. Commun.* **4**, 2890 (2013).
17. J. Chen, M. Badioli, P. Alonso-González, S. Thongrattanasiri, F. Huth, J. Osmond, M. Spasenović, A. Centeno, A. Pesquera, P. Godignon, A. Z. Elorza, N. Camara, F. J. García de Abajo, R. Hillenbrand, and F. H. L. Koppens, "Optical nano-imaging of gate-tunable graphene plasmons," *Nature* **487**(7405), 77–81 (2012).
18. Z. Fei, A. S. Rodin, G. O. Andreev, W. Bao, A. S. McLeod, M. Wagner, L. M. Zhang, Z. Zhao, M. Thiemens, G. Dominguez, M. M. Fogler, A. H. Castro Neto, C. N. Lau, F. Keilmann, and D. N. Basov, "Gate-tuning of graphene plasmons revealed by infrared nano-imaging," *Nature* **487**(7405), 82–85 (2012).
19. L. Novotny and B. Hecht, *Principles of Nano-Optics* (Cambridge University, 2012).
20. C. Huber, A. Trügler, U. Hohenester, Y. Prior, and W. Kautek, "Optical near-field excitation at commercial scanning probe microscopy tips: a theoretical and experimental investigation," *Phys. Chem. Chem. Phys.* **16**(6), 2289–2296 (2014).
21. A. J. Huber, J. Wittborn, and R. Hillenbrand, "Infrared spectroscopic near-field mapping of single nanotransistors," *Nanotechnology* **21**(23), 235702 (2010).
22. Z. Fei, G. O. Andreev, W. Bao, L. M. Zhang, A. S. McLeod, C. Wang, M. K. Stewart, Z. Zhao, G. Dominguez, M. Thiemens, M. M. Fogler, M. J. Tauber, A. H. Castro-Neto, C. N. Lau, F. Keilmann, and D. N. Basov, "Infrared nanoscopy of Dirac plasmons at the graphene-SiO₂ interface," *Nano Lett.* **11**(11), 4701–4705 (2011).
23. J. M. Stiegler, Y. Abate, A. Cvitkovic, Y. E. Romanyuk, A. J. Huber, S. R. Leone, and R. Hillenbrand, "Nanoscale infrared absorption spectroscopy of individual nanoparticles enabled by scattering-type near-field microscopy," *ACS Nano* **5**(8), 6494–6499 (2011).
24. J. M. Hoffmann, B. Hauer, and T. Taubner, "Antenna-enhanced infrared near-field nanospectroscopy of a polymer," *Appl. Phys. Lett.* **101**, 193105 (2012).
25. S. Amarie, T. Ganz, and F. Keilmann, "Mid-infrared near-field spectroscopy," *Opt. Express* **17**(24), 21794–21801 (2009).
26. F. Huth, A. Govyadinov, S. Amarie, W. Nuansing, F. Keilmann, and R. Hillenbrand, "Nano-FTIR absorption spectroscopy of molecular fingerprints at 20 nm spatial resolution," *Nano Lett.* **12**(8), 3973–3978 (2012).
27. S. Amarie, P. Zaslansky, Y. Kajihara, E. Griesshaber, W. W. Schmahl, and F. Keilmann, "Nano-FTIR chemical mapping of minerals in biological materials," *J. Nanotechnol.* **3**, 312–323 (2012).
28. P. Hermann, A. Hoehl, P. Patoka, F. Huth, E. Rühl, and G. Ulm, "Near-field imaging and nano-Fourier-transform infrared spectroscopy using broadband synchrotron radiation," *Opt. Express* **21**(3), 2913–2919 (2013).
29. P. Hermann, A. Hoehl, G. Ulrich, C. Fleischmann, A. Hermelink, B. Kästner, P. Patoka, A. Hornemann, B. Beckhoff, E. Rühl, and G. Ulm, "Characterization of semiconductor materials using synchrotron radiation-based near-field infrared microscopy and nano-FTIR spectroscopy," *Opt. Express* **22**(15), 17948–17958 (2014).
30. H. A. Bechtel, E. A. Muller, R. L. Olmon, M. C. Martin, and M. B. Raschke, "Ultrabroadband infrared nanospectroscopic imaging," *Proc. Natl. Acad. Sci. U.S.A.* **111**(20), 7191–7196 (2014).
31. F. Huth, M. Schnell, J. Wittborn, N. Ocelic, and R. Hillenbrand, "Infrared-spectroscopic nanoimaging with a thermal source," *Nat. Mater.* **10**(5), 352–356 (2011).
32. J. Faist, F. Capasso, D. L. Sivco, C. Sirtori, A. L. Hutchinson, and A. Y. Cho, "Quantum cascade laser," *Science* **264**(5158), 553–556 (1994).
33. A. Hugi, R. Maulini, and J. Faist, "External cavity quantum cascade laser," *Semicond. Sci. Technol.* **25**(8), 083001 (2010).
34. E. Yoxall, M. Navarro-Cia, M. Rahmani, S. A. Maier, and C. C. Phillips, "Widely tuneable scattering-type scanning near-field optical microscopy using pulsed quantum cascade lasers," *Appl. Phys. Lett.* **103**(21), 213110 (2013).
35. B. Pollard, E. A. Muller, K. Hinrichs, and M. B. Raschke, "Vibrational nano-spectroscopic imaging correlating structure with intermolecular coupling and dynamics," *Nat. Commun.* **5**, 3587 (2014).
36. A. Hasenkamp, N. Kröger, A. Schönhal, W. Petrich, and A. Pucci, "Surface-enhanced mid-infrared spectroscopy using a quantum cascade laser," *Opt. Express* **23**(5), 5670–5680 (2015).
37. I. M. Craig, M. S. Taubman, A. S. Lea, M. C. Phillips, E. E. Josberger, and M. B. Raschke, "Infrared near-field spectroscopy of trace explosives using an external cavity quantum cascade laser," *Opt. Express* **21**(25), 30401–30414 (2013).

38. A. A. Govyadinov, I. Amenabar, F. Huth, P. S. Carney, and R. Hillenbrand, "Quantitative measurement of local infrared absorption and dielectric function with tip-enhanced near-field microscopy," *J. Phys. Chem. Lett.* **4**(9), 1526–1531 (2013).
39. J. Sun, J. C. Schotland, R. Hillenbrand, and P. S. Carney, "Nanoscale optical tomography using volume-scanning near-field microscopy," *Appl. Phys. Lett.* **95**(12), 121108 (2009).
40. A. A. Govyadinov, S. Mastel, F. Golmar, A. Chuvilin, P. S. Carney, and R. Hillenbrand, "Recovery of permittivity and depth from near-field data as a step toward infrared nanotomography," *ACS Nano* **8**(7), 6911–6921 (2014).
41. N. Ocelic, A. Huber, and R. Hillenbrand, "Pseudoheterodyne detection for background-free near-field spectroscopy," *Appl. Phys. Lett.* **89**(10), 101124 (2006).
42. B. Knoll and F. Keilmann, "Enhanced dielectric contrast in scattering-type scanning near-field optical microscopy," *Opt. Commun.* **182**(4-6), 321–328 (2000).
43. P. G. Gucciardi, G. Bachelier, and M. Allegrini, "Far-field background suppression in tip-modulated apertureless near-field optical microscopy," *J. Appl. Phys.* **99**(12), 124309 (2006).
44. B. Stuart, "Infrared spectroscopy," in *Kirk-Othmer Encyclopedia of Chemical Technology*, John Wiley & Sons, Inc., ed. (John Wiley & Sons, Inc., 2005).
45. P. Werle, F. Slemr, K. Maurer, R. Kormann, R. Mücke, and B. Jänker, "Near- and mid-infrared laser-optical sensors for gas analysis," *Opt. Lasers Eng.* **37**(2-3), 101–114 (2002).
46. P. S. Carney, B. Deutsch, A. A. Govyadinov, and R. Hillenbrand, "Phase in nanooptics," *ACS Nano* **6**(1), 8–12 (2012).
47. G. Zhang and D. Wang, "Colloidal lithography--the art of nanochemical patterning," *Chem. Asian J.* **4**(2), 236–245 (2009).
48. W. Nuansing, D. Frauchiger, F. Huth, A. Rebollo, R. Hillenbrand, and A. M. Bittner, "Electrospinning of peptide and protein fibres: approaching the molecular scale," *Faraday Discuss.* **166**, 209–221 (2013).
49. S. Mastel, A. A. Govyadinov, T. V. A. G. de Oliveira, I. Amenabar, and R. Hillenbrand, "Nanoscale-resolved chemical identification of thin organic films using infrared near-field spectroscopy and standard Fourier transform infrared references," *Appl. Phys. Lett.* **106**(2), 023113 (2015).

1. Introduction

Scattering-type scanning near-field optical microscopy (s-SNOM) [1] has emerged as a powerful tool for optical and infrared imaging at significantly sub-diffraction-limited length scales, and has been applied to diverse range of research topics including polymer studies [2–4], phonons [5,6], nanoscale free-carrier densities [7], plasmonics [8–12], biological materials [13–16] and graphene [17,18]. It is particularly effective when operated with mid-infrared (IR) radiation, as in this "chemical fingerprint" spectral region the vibrational modes of molecules can be probed to provide non-destructive analysis of a sample's chemical composition. The resolution of traditional infrared-spectroscopic techniques is constrained to around half of the light's wavelength (typically $\sim 5 \mu\text{m}$) by the diffraction limit. S-SNOM, on the other hand, circumnavigates this limit by making use of the enhanced and strongly confined near field that exists at the apex of illuminated sharp probes [19,20]. As a result, infrared near-field images and spectra can be obtained with a spatial resolution that is determined by the size of the probe's apex (typically $\sim 25 \text{ nm}$).

To date, the majority of spectroscopic measurements made with s-SNOM have been performed in one of two ways; either by extracting the pixel values of a sequence of consecutively recorded single wavelength images [2,3,5,21–24] or by using a broadband light source, such as a femtosecond-pulsed lasers [25–27], synchrotrons [28–30] or globars [31], to perform Fourier transform spectroscopy at individual pixels (nano-FTIR). The former can be time consuming in both data acquisition and post-processing whereas the latter's light sources tend to suffer from low spectral irradiance leading to long measurement times and low spectral resolution.

An alternative approach is to use the spectral tunability and high powers offered by contemporary external cavity quantum cascade lasers (QCLs) [32,33]. These lasers offer the advantage of being able to perform single wavelength imaging [16,34,35], while also being able to "sweep" through their tuning range to gather a full spectrum at any particular point of interest [36]. Previous publications on near-field spectroscopy with a swept QCL source have shown that it is possible to rapidly distinguish substances on a sample surface using such a wavelength-sweep [37], but until now no demonstration has been made in which *both* the magnitude and phase of the near-field signal have been measured via a swept laser source. Both values are required for a number of important applications; the reconstruction of the

sample's local dielectric constant [38], near-field tomography [39,40] and, critically for nanoscale chemical identification, the ability to directly compare spectra gathered in the near field with traditionally acquired far-field absorption spectra [26].

This link between the near-field and far-field spectra is due to the fact that the imaginary part of the near-field signal (as measured by s-SNOM) matches well with far-field absorbance spectra [38] in the case of weak molecular oscillators, for example most polymers and biological materials. Weak oscillators are characterized by a strictly positive real part of the dielectric constant, $\text{Re}(\epsilon) > 0$, throughout a spectral region of resonant absorption [3]. Given the prevalence of standard infrared spectroscopy tools (such as Fourier transform infrared spectroscopy, or FTIR), large databases of infrared absorption spectra exist. With magnitude and phase-resolved near-field spectroscopy, these same databases could be used in the future for material identification by simply searching for the particular absorbance spectrum that best fits the imaginary part of the near-field spectrum. Using the imaginary part in this way, however, requires that both the magnitude and phase of the near-field signal are recorded.

2. Experimental

2.1. S-SNOM setup

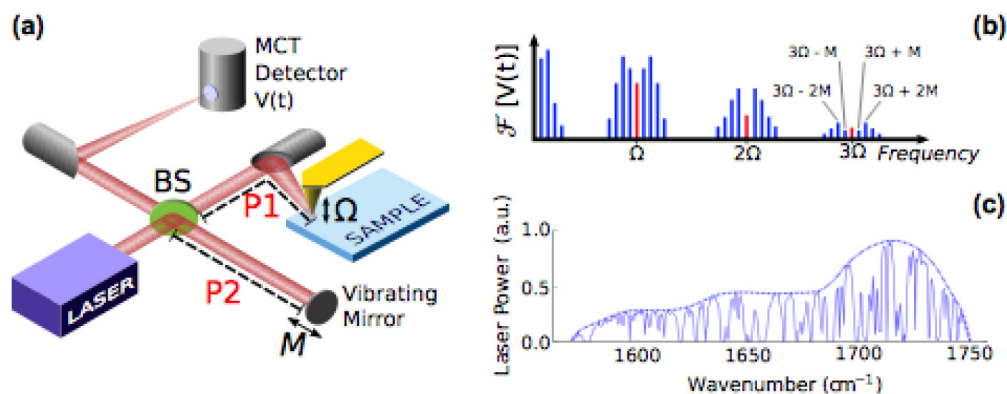


Fig. 1. (a) Schematic of the pseudo-heterodyne detection technique as employed for wavelength-swept spectroscopy. Light from a laser passes through a beamsplitter (BS) where it splits into two arms. In the signal arm (path length labeled P1), the light is focused at a sharp oscillating probe (frequency Ω) that also acts to backscatter the light for collection at the detector. In the reference arm (path length P2), the light is phase modulated by reflection from a vibrating mirror (frequency M where $M \ll \Omega$). The effect of interfering the two beams is shown in (b), a representation of the Fourier transform of the time dependent waveform $V(t)$ gathered at the mercury-cadmium-telluride (MCT) infrared detector (not to scale). Peaks at the harmonics of the probe oscillation Ω are split into sidebands separated by the mirror vibration frequency M . The magnitude and phase of the near-field signal can be deduced from the odd and even sidebands of a suitably high harmonic (labeled here as $3\Omega \pm M$ and $3\Omega \pm 2M$ respectively). (c) Power spectrum of our QCL (solid line) over its tuning range of 1570 to 1750 cm^{-1} . The sharp dips in power are caused by atmospheric water absorption peaks. Also shown is a guide to the eye (dashed line) where the water absorption is ignored.

Our experimental setup is based on the widely used pseudo-heterodyne detection scheme [41] as implemented on a commercially available s-SNOM (*NeaSNOM*, *Neaspec*), a schematic for which is shown in Fig. 1(a). In more detail, continuous wave (CW) light emitted by the QCL (*CW-PLS Laser*, *Daylight Solutions*) passes through a beamsplitter where it forms two beams. The first beam – the *signal arm* – continues to an off-axis parabolic mirror where it is focused to the apex of an oscillating metallic probe (oscillation frequency Ω typically in the hundreds of kilohertz) which acts as an optical antenna by both confining, and subsequently scattering, the field in its immediate vicinity. The same parabolic mirror collects and re-collimates the backscattered light. The second beam – the *reference arm* – is phase modulated by reflection from a vibrating mirror (oscillation frequency M typically a few hundred hertz). Both arms are

recombined and focused on to a nitrogen-cooled mercury-cadmium-telluride (MCT) detector (*FTIR-16-0.1, Infrared Associates*).

The light that is backscattered from the probe is made up of two complex coefficients: the near-field signal σ_{NF} and the background scattering σ_B [1] as shown in Eq. (1):

$$E_{sca} = (\sigma_{NF} + \sigma_B)E_{in} \quad (1)$$

E_{sca} and E_{in} represent the scattered and incident fields respectively. The near-field signal σ_{NF} relates to the scattered near field that has been modified by the interaction between the probe's apex and sample (thus encoding information about the local optical properties of the sample surface), while the background scattering σ_B represents the field scattered by the sample or body of the probe and remains unaffected by the near-field interaction. The two components can be distinguished by their probe-sample separation dependence; the near-field signal σ_{NF} typically vanishes with a separation of a few tens of nanometers, while the background σ_B varies only slightly. As a result of the probe's vertical oscillation (typically a few tens of nm at frequency Ω), most of the high-frequency time variation in the detector waveform $V(t)$ is due to changes in the near-field interaction signal, and not the background which remains relatively constant. Consequently, by Fourier transforming the time trace of the detector signal over a short integration time (~ 10 ms) and measuring at a suitably high harmonic of the probe vibration frequency $n\Omega$, background can be reduced [42,43]. To extract the background-free magnitude and phase of σ_{NF} , we use the sidebands created by the reference mirror's vibration M , the amplitude of which is dictated by the wavelength [41]. These sidebands appear around the harmonics of Ω , as shown in Fig. 1(b) (where they are labeled $3\Omega + M$, $3\Omega + 2M$ etc.) The complex near-field signal can be calculated from the values of two adjacent sidebands. Taking into account the higher harmonic demodulation, we denote the near-field signal as σ_n , where n represents any harmonic at which the background scattering provides a negligible contribution. For the experiments that follow, a probe oscillation amplitude of 50nm was used, for which the background scattering was fully suppressed at the third harmonic ($n = 3$).

Figure 1(c) shows the power spectrum of our QCL. Its tuning range stretches from 1570 to 1750 cm^{-1} , which is a spectral region of particular importance for the identification of biological materials [44]. It is also a region in which atmospheric water absorbs strongly at multiple wavelength [45]; for this reason numerous dips are visible. At these transmission minima very little power reaches the s-SNOM probe meaning that there are gaps in the recorded near-field spectra $\sigma_3(\lambda)$. Such gaps do not tend to prevent material identification, however, as will be seen later in this paper. Furthermore, it should be noted that these gaps are not unique to the swept-wavelength technique; they are problematic for all forms of infrared spectroscopy. In future implementations the atmospheric water absorption could be circumvented by encapsulating the whole setup and filling it with dry air or pure nitrogen.

2.2. Pseudo-heterodyne spectroscopy: single wavelength imaging and wavelength sweeping

For spectroscopic measurements, the pseudo-heterodyne scheme can be employed in one of two ways. The first way – as has been employed previously – is based on imaging. A single laser wavelength is selected and the sample is raster scanned beneath the probe by a high precision piezoelectric stage. As such, an image is built up pixel by pixel, and if a number of images are taken at different wavelengths, the spectral characteristics of a particular feature can be extracted from its pixel values. The second way is what we introduce in this paper, where we position the probe at a single point and we sweep the laser's wavelength through a spectral range of interest. If the rate of change of wavelength is constant, the elapsed time from the start of the sweep can be directly equated to the lasing wavelength. In this way, we can measure the complex near-field spectrum at a single pixel, $\sigma_3(\lambda)$ – which is comprised of both a magnitude spectrum, $s_3(\lambda)$, and a phase spectrum, $\phi_3(\lambda)$ – within a few seconds.

Both the single wavelength imaging approach and the wavelength sweeping approach also require a reference spectrum, $\sigma_{3,ref}(\lambda)$, to be acquired. The reference spectrum accounts for variations in laser power at different wavelengths, as well as changes caused by other

wavelength-sensitive components of the experimental setup. In the imaging approach, this is usually achieved by placing the sample on a spectrally flat substrate such as gold or silicon such that both the sample $\sigma_{3,\text{sample}}(\lambda)$ and reference $\sigma_{3,\text{ref}}(\lambda)$ spectra can be extracted from the series of single wavelength pictures. For the experiments in this paper, we position the probe above either the sample or reference material, and sweep the laser's wavelength at each to gather the relevant spectrum. For brevity, we denote the normalized near-field spectra $\sigma_{3,\text{sample}}(\lambda)/\sigma_{3,\text{ref}}(\lambda)$ as $\eta_3(\lambda)$.

Temporarily disregarding the characteristics of the laser itself, the spectral resolution of a spectrum recorded by a wavelength sweep is defined by the interplay between two parameters; the rate at which the laser changes wavelength, and the integration time of the pseudo-heterodyne technique. The experiments contained in this paper used sweep rates of approximately $20 \text{ cm}^{-1}/\text{s}$ and integration times of 6.5 ms (a value limited by the oscillation frequency of the reference mirror, in our case the commercial *Neaspec PMDK-2 module*), corresponding to a nominal spectral resolution of around 0.13 cm^{-1} . As will be seen in the following section, however, difficulties in perfectly replicating sweeps – as well as signal-to-noise considerations – lead us to average over a number of data points for an actual spectral resolution of around 2 cm^{-1} .

2.3. Importance of the white light position

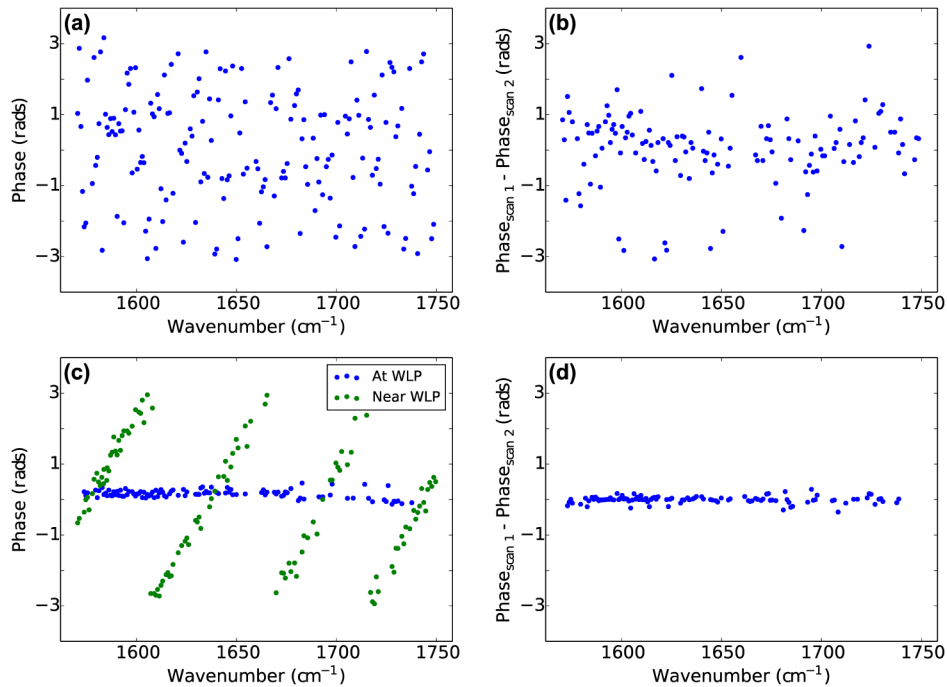


Fig. 2. (a) Near-field phase spectrum $\phi_3(\lambda)$ of a single QCL wavelength sweep on a silicon surface where the path length difference is large ($>2 \text{ cm}$). (b) A repeatability test of two sweeps with a large path length difference ($>2 \text{ cm}$). In a perfectly repeatable measurement, the phase of one spectrum subtracted from the phase of another would be zero. (c) The same measurement as (a), but with the path length difference small (green dots) and zero (blue dots). The propagation phase ramping caused by the wavelength-path difference dependence of Eq. (3) is clearly visible in the case close to the white light position (WLP). Data at low power wavelengths have been removed for clarity. (d) Repeatability test performed at the white light position.

A single near-field phase spectrum, $\phi_3(\lambda)$, of a silicon surface recorded with a wavelength sweep covering the entire tuning range of our QCL, is shown in Fig. 2(a). The reference

mirror oscillation amplitude was adjusted for the central wavelength of 1660 cm^{-1} . It is clear that the spectrum has a large distribution of values. This spread can be understood by looking at the different contributions to the measured near-field phase, $\phi_3(\lambda)$, as shown in Eq. (2):

$$\phi_3(\lambda) = \phi_{\text{NF}}(\lambda) + \phi_{\text{PROP}}(\lambda) \quad (2)$$

$\phi_{\text{NF}}(\lambda)$ represents the contribution of the near-field interaction between the probe and the sample (which is a constant value for a spectrally flat material such as silicon and can hence be neglected in this discussion) and $\phi_{\text{PROP}}(\lambda)$ represents the contribution which arises from the difference in propagation length between the two arms of the interferometer (the *propagation phase*) [46]. The latter is related to the wavelength as shown in Eq. (3):

$$\phi_{\text{PROP}} = \frac{2\pi}{\lambda} 2d \quad (3)$$

The path length difference of the two arms (path lengths labeled P1 and P2 in Fig. 1(a)) is denoted d . For the measurements in Fig. 2(a) and (b), d was set to 2 cm, a typical value for an unmodified commercial s-SNOM (*NeaSNOM*, *Neaspec*). With this relatively large path difference, the change in the measured phase between wavelengths is also large. This means that as the wavelength is swept, $\phi_{\text{PROP}}(\lambda)$ introduces a very fast phase ramp that obscures entirely $\phi_{\text{NF}}(\lambda)$. A wavelength change of 0.5 cm^{-1} , for example, leads to a phase jump of 4π in $\phi_{\text{PROP}}(\lambda)$. The propagation phase, therefore, explains the broad distribution of the measured values of $\phi_3(\lambda)$ between $-\pi$ and π in Fig. 2(a).

In theory, the large spread of a near-field spectrum is not problematic; all s-SNOM measurements must be normalized. If the laser sweep was perfectly reproducible, each point within the spectrum would have exactly the same propagation phase $\phi_{\text{PROP}}(\lambda)$ from sweep to sweep – the propagation phases should cancel, and the remaining phase of the normalized spectrum $\eta_3(\lambda)$ should depend purely on the near-field interaction $\phi_{\text{NF}}(\lambda)$ between the probe and the sample. Figure 2(b) shows the results of a repeatability test, in essence a normalization of one spectrum on silicon to another. Although the spread of values is smaller in this “normalized” case than in that of a single sweep, the range of values is still big, and this would mask all but the biggest of changes in $\phi_{\text{NF}}(\lambda)$, which is fundamentally what we want to measure. Such an inability to reproduce the near-field phase spectrum $\phi_3(\lambda)$ in two identical measurements on silicon suggests a lack of repeatability in the wavelength sweep of our QCL – the lasing wavelength at any given moment varies slightly from sweep to sweep, and these small fluctuations in the wavelength introduce non-reproducible variations in the propagation phase.

Taking the numerical value of the spread of phase values in the repeatability test of Fig. 2(b) (~ 2 radians), we can use Eq. (3) to calculate the uncertainty in the lasing wavelength as approximately 0.08 cm^{-1} . We suggest that this wavelength uncertainty is likely caused by the mechanical nature in which the wavelength is tuned. Our laser is arranged in an external cavity configuration [33], meaning that the wavelength is selected by use of an angled diffraction grating as part of the laser cavity. A stepper motor with a non-zero repositioning error controls the angle of this diffraction grating, and as such, no two wavelength sweeps are precisely alike. This repositioning error, therefore – when coupled with a large interferometer path length difference – is the root cause of the unrepeatability of the near-field phase spectra $\phi_3(\lambda)$.

It should be emphasized that the near-field phase spectrum is unrepeatable because of the contribution of the propagation phase, $\phi_{\text{PROP}}(\lambda)$, and not the near-field interaction, $\phi_{\text{NF}}(\lambda)$, which does not change significantly within a single wavelength step. Significant improvements in repeatability can be made, therefore, by reducing the dependence of the propagation phase on the wavelength. By moving the interferometer to its white light position (i.e. equal path lengths or $d = 0$), the recorded phase can be made entirely independent of the

wavelength for a spectrally flat material (as seen from Eq. (3)). This can be seen in the Fig. 2(c), which shows another single phase spectrum, $\phi_3(\lambda)$, on silicon where the path length was set small (green dots) and zero (blue dots). With a small difference, a regular ramp is observed as the phase cycles from $-\pi$ to π several times during the sweep, while at the white light position itself, the phase is completely decoupled from the wavelength and remains at a constant value. When another repeatability test is performed at $d = 0$ as shown in Fig. 2(d), it is clear that slight differences in the wavelength from sweep to sweep no longer lead to a broad distribution of phases, and two separate measurements can be reliably matched as sample and reference spectra during the calculation of the normalized near-field spectrum $\eta_3(\lambda)$. We note that the silicon surface will be covered by a natural oxide layer several nanometers thick. As this oxide layer does not absorb in the spectral range covered by our laser, the “silicon’s” response remains spectrally flat, and is thus suitable for use as a reference spectrum.

3. Results

3.1. PMMA discs

As a proof-of-principle experiment that our wavelength sweeping technique is capable of collecting high-resolution infrared absorption spectra, we first present the results from a simple sample – a polymer disc (poly-(methyl methacrylate), or PMMA) on a silicon substrate prepared by colloidal lithography [47] – and compare them to a “traditional” near-field spectrum gathered from a series of single wavelength images (e.g [3]). PMMA is known to absorb strongly near 1730 cm^{-1} due to C = O bond stretching, and so we expected to see a peak in the imaginary part of $\eta_3(\lambda)$ at these wavelengths. The studied disc was slightly under 20nm in height, and 100nm in diameter, as can be seen in the topography of Fig. 3(a).

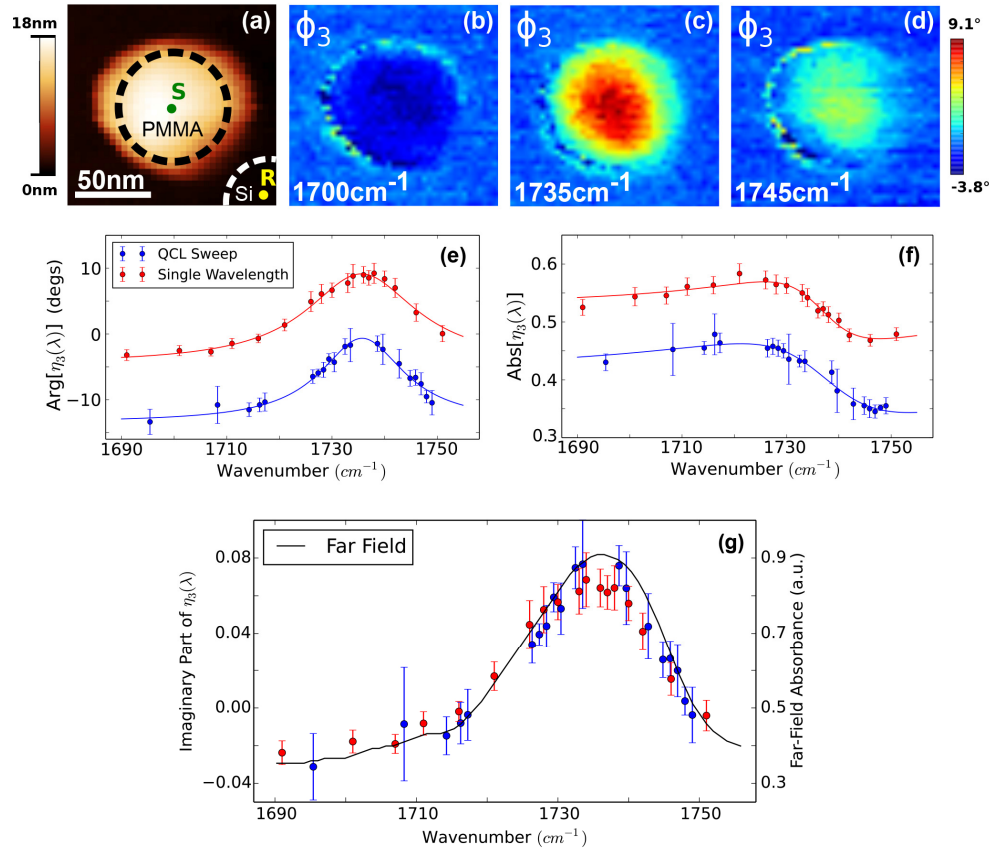


Fig. 3. (a) The topography of an 18nm thick PMMA disc. The dashed circles indicate the areas for which the pixel values were averaged to find the sample and reference spectra for the single wavelength images. The green ‘S’ and the yellow ‘R’ indicate the positions at which the QCL sweep sample and reference spectra were taken respectively. (b)-(d) A selection of the near-field phase ϕ_3 images of the same disc taken at 1700, 1735 and 1745 cm^{-1} respectively, where the phase on silicon has been set to zero. (e)-(g) The normalized phase, magnitude and imaginary part spectra extracted from a series of single wavelength images (red) and our QCL sweeping technique (blue). For clarity, the wavelength swept curves have been offset by -10 degrees and -0.1 in the phase and magnitude spectra respectively. The solid blue and red lines are Lorentzian curve fits – these are not intended to be precise representations of the underlying data but rather guides to the eye. The two curves in the imaginary part (g) – which is directly comparable to the local far-field absorption [38] – have been overlaid to show their agreement. Also shown in (g) is the grazing incidence Fourier transform infrared (GI-FTIR) absorption spectrum of an 8nm PMMA film (black line, plotted on right y-axis) which has a spectral resolution of 2 cm^{-1} .

Panels 3(b)-3(d) show the near-field phase ϕ_3 of single wavelength measurements at 1700, 1735 and 1745 cm^{-1} . These phase data are shown because they indicate the local absorption [38]. As expected, the images clearly show stronger contrast close to the C = O absorption peak with a maximum phase contrast of 9° (as compared to the silicon substrate) at 1735 cm^{-1} . The red curves in panels 3(e)-3(g) show the magnitude, phase and imaginary parts respectively of the normalized near-field signal $\eta_3(\lambda)$. Their values are extracted by averaging over the pixels containing the PMMA and the substrate in each image as outlined in the topography image Fig. 3(a) by a dashed circle. The error bars show the standard deviation of the pixel values used in the averaging.

The blue curves in Fig. 3(e) and 3(f) are found using the wavelength sweeping method. For these measurements the laser was swept from 1690 to 1750 cm^{-1} a total of 30 times while

the probe was on the PMMA, and 20 times on the silicon. Every sweep took 2.8 seconds meaning a total measurement time of slightly less than 2.5 minutes. To extract the near-field spectrum $\sigma_3(\lambda)$, the sweeps were first divided up into time bins of 70 ms (corresponding to a spectral resolution of 1.5 cm^{-1} as a number of wavelength steps occur within the bin). The value of each time bin – also corresponding to a wavelength – was calculated by finding the median average of the pseudo-heterodyne measurements within it. The mean and standard deviation of each bin was then found by combining the individual sweeps (i.e. 30 on PMMA, 20 on silicon), leaving a single spectrum for each material with a measure of the error at each wavelength $\sigma_3(\lambda) \pm \text{err}(\lambda)$. Next, the PMMA spectrum was normalized to the silicon spectrum and the magnitude, phase and imaginary parts of $\eta_3(\lambda)$ extracted. Finally, data points where the phase error bars exceeded 8° were excluded for visual clarity, resulting in blank areas in the spectrum.

In Fig. 3(g) – where the imaginary parts of the individual images and the wavelength sweeping method are overlaid – close agreement is seen, proving that the wavelength sweeping technique is effective for rapidly gathering near-field spectra. The slightly lower peak in the single wavelength spectrum is likely due to averaging over an area of non-uniform PMMA height leading to a variation in the strength of the local absorption. In both cases, the peak maximum at 1735 cm^{-1} shows excellent agreement with the far-field absorption spectrum, which was taken using grazing incidence Fourier transform infrared spectroscopy (GI-FTIR). It is also evident that some wavelengths that are accessible in single wavelength imaging exhibit large measurement errors in the wavelength sweeping spectra; we speculate that this is due to an insufficient laser settling time during the sweep causing either a low or a highly variable power output.

We also note that using a constant reference mirror vibration amplitude during the wavelength sweep introduces a systematic error to the measurement [41]. It can be minimized by adjusting the vibration amplitude for the central wavelength of the sweep; the error is largest at the spectral extremes. For the tuning range of our laser, however, its effect is negligibly small, as can be seen from the excellent agreement of the wavelength-swept spectra with both the single wavelength spectra (where the reference mirror vibration amplitude was adjusted for each wavelength) and with the GI-FTIR data.

Finally, we offer a comment about the y scale of Fig. 3(g); it may seem counter-intuitive that the imaginary part of the normalized near-field spectrum $\eta_3(\lambda)$ can have negative values. These negative values stem from the relative phases of the sample and reference spectra. When the measured near-field phase, ϕ_3 , of silicon is larger than that of the PMMA (i.e. between 1690 and 1720 cm^{-1}) then the normalization procedure yields a negative value for the phase which, in turn, leads to a negative imaginary part of $\eta_3(\lambda)$. This is clearly seen in the phase spectrum of Fig. 3(e) and the single wavelength image at 1700 cm^{-1} in Fig. 3(b). Physically, this means that the probe-surface interaction for silicon introduces a slightly larger phase delay in the scattered light than that for PMMA (for off-resonant wavelengths). Speculatively, we suggest that the reason for this delay could be either a shift in the antenna resonance of the probe as it is loaded upon approaching the surface, or because the tip is also illuminated by reflection from the sample (as well as direct illumination) and hence can be affected by sample topography [46]. For the purposes of the normalization, however, it is only required that the near-field phase response of the silicon be spectrally flat. Its absolute value (i.e. whether it is greater or less than the near-field phase response of PMMA) is inconsequential, and only matters insofar as dictating the sign of the normalized spectrum.

3.2. Distinguishing “unknown” organic fibers

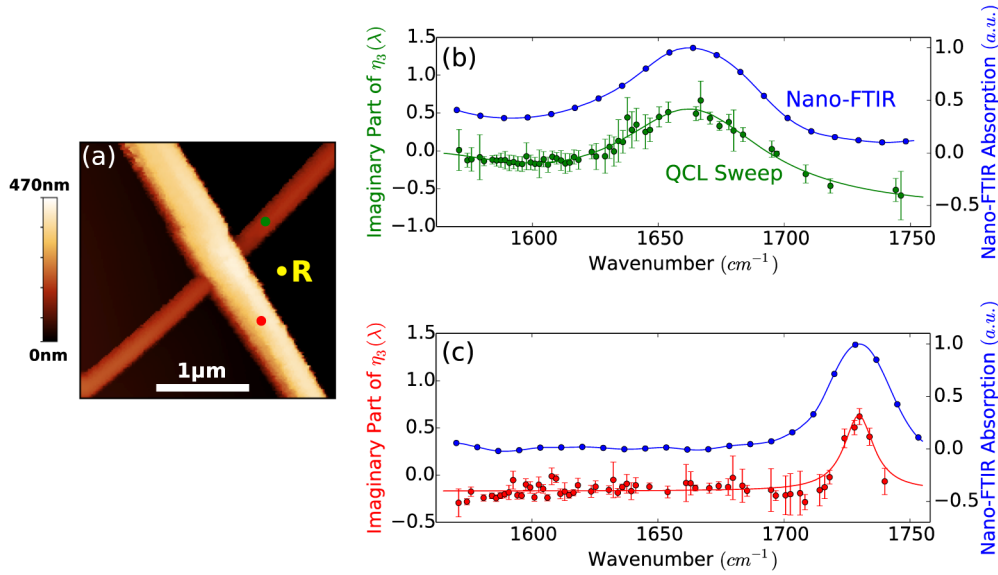


Fig. 4. (a) Topography of two fibers. (b,c) The imaginary parts of normalized near-field spectra taken at the green and red dots respectively (averaged over 10 sweeps at each point). The normalization spectrum was recorded at the yellow dot labeled ‘R’ and was averaged over 5 sweeps. The solid lines are Lorentzian curve fits – these are not intended to be precise representations of the underlying data but rather guides to the eye. The blue dots are nano-FTIR absorption spectra [26] taken from a similar (but not the same) protein fibril (b) and a 174nm PMMA film (c) with an 8 cm^{-1} spectral resolution. The blue lines represent the zero-filled spectra.

In finishing, we use the wavelength sweeping technique to identify different materials on a sample surface. PMMA and protein fibers were prepared by electrospinning [48] and placed on a silicon substrate. Figure 4(a) shows a crossing of two fibers, but it is impossible to identify them chemically from their topography alone. To do so, we took 10 sweeps at locations marked by green and red dots over the full range of our QCL (1570 to 1750 cm^{-1}) and 5 normalization sweeps on the silicon substrate at the location marked with a yellow ‘R’.

The same procedure as above was followed for extracting the normalized spectra $\eta_3(\lambda)$ with a 2 cm^{-1} spectral resolution, and the imaginary parts are shown in panels 4(b) and 4(c). By comparing these near-field spectra to far-field absorption spectra, it is a simple task to identify the two fibers as PMMA (top-left to bottom-right) and protein (bottom-left to top-right) via their absorption peaks at 1730 cm^{-1} and 1660 cm^{-1} respectively (the former corresponding to the previously examined C = O stretching mode and the latter to the Amide I peak present in biological materials). The different thickness of PMMA accounts for the spectral shift of the peak relative to the measurements in Fig. 3 [49]. The total measurement time for each of these spectra was, again, slightly less than 2.5 minutes.

Also shown in panels 4(b) and 4(c) are nano-FTIR absorption spectra. These were not recorded at the same positions as marked in panel (a) and as such are not intended for quantitative comparison with the QCL sweep spectra. Instead, they were recorded on a similar (but not identical) protein fiber and a 174nm film of PMMA respectively. Similar peak positions between the nano-FTIR and QCL sweep methods, however, provide further qualitative evidence for the effectiveness of wavelength-swept spectroscopy.

4. Conclusion

In conclusion, we have demonstrated a method of rapidly gathering high-resolution, near-field spectra by combining the well-established pseudo-heterodyne detection technique with a wavelength-swept QCL. This allows for magnitude and phase-resolved measurement of the complex near-field signal σ_3 . This gives us access to the imaginary part of σ_3 , which, in turn, permits direct comparison with far-field absorption spectra.

We have also found that the interferometer used for pseudo-heterodyne detection must be set up in the white light position (so that the path length difference between the signal and reference arms is zero). This prevents the unrepeatability of the small wavelength steps that constitute our laser's wavelength sweep from drastically affecting the normalized near-field spectrum $\eta_3(\lambda)$ by removing the dependence of the measured phase, ϕ_3 , on the wavelength (excluding any spectral variations in the phase caused by the probe-sample interaction).

The spectral region covered by our QCL (1570 to 1750 cm^{-1}) is plagued by atmospheric water absorption peaks, and improvements could be made to the quality of our measurements by recording spectra in a pure nitrogen or dry air environment; this would remove the gaps in the spectral coverage. The systematic error introduced by the constant reference mirror vibration amplitude, although negligible for our QCL, would become significant for lasers capable of sweeping through a bigger range of wavelengths. By varying the mirror vibration during the sweep, however, this systematic error could be completely eliminated. Finally, we note that the use of the white light position might enable unstable QCLs (or other lasers that may have unrepeatable tuning characteristics) to be used in other types of interferometric setup – both in the near field and the far field. It also benefits monochromatic phase imaging by preventing small instabilities in the lasing wavelength from producing artificial phase modulations.

Acknowledgments

The authors would like to thank Thales De Oliveira and Wiwat Nuansing for preparing the PMMA disc and fibril samples respectively, Roman Krutovostovs for providing the GI-FTIR spectra, Iban Amenabar and Alexander Govyadinov for providing the nano-FTIR spectra and Scott Carney for his stimulating input. Funding for this research is gratefully acknowledged from ERC Starting Grant No. 258461 (TERATOMO).